Supplementary material:

Predicting Sizes of Droplets made by Microfluidic Flow-induced Dripping

Randall M. Erb,[1,*] Dominik Obrist,[2] Philipp W. Chen,[1] Julia Studer,[1] André R. Studart[1,†]

[1] *Complex Materials, Department of Materials, ETH Zürich, 8093 Zürich, Switzerland*

[2] *Institute of Fluid Dynamics, ETH Zürich, 8092 Zürich, Switzerland*

I. Fabrication of Glass Microcapillary Devices

Glass microcapillary devices were produced following the original procedure by Utada *et al* [1] (Figs 1 and 3, main manuscript). To fabricate such devices, a tapered cylindrical inlet capillary is first fitted into an outer square capillary. A second tapered cylindrical collector capillary is then inserted from the other side into the same outer square capillary and positioned such that the distance between the two tapered capillaries is fixed at 100 μm. Circular borosilicate glass capillaries were purchased from Harvard Apparatus, Holliston, MA, and square glass capillaries were purchased from World Precision Instruments, Inc., Sarasota, FL. A square capillary with inner diameter of 1.1 mm and cylindrical inlet and collector capillaries with outer diameter of 1.0 mm were used to enable easy assembly, while maintaining a good alignment of the capillaries. Microcapillary tips were made by pulling the thin-walled glass capillaries (P-97 Micropipette Puller, Sutter Instrument) and breaking them to a desired tip diameter using a microforge (MF-830, Narishige). Capillaries with initial inner diameters of either 580 or 200 μm were used. For single dripping experiments, the heating conditions were adjusted to produce inlet capillaries with inner diameters varying from 20.6 to 47.4 μm at the tip. Likewise, the inner diameter of the collector capillaries was varied from 45.0 to 559 μm at the tip. The microcapillary system used for the multiple dripping experiments had an inner capillary tip of 22 μm and a collector capillary of 202 μm. Capillary dimensions were measured end-on in an optical microscope to avoid optical artifacts due to the capillary curvature that can distort orifice measurements by up to 30%.

II. Dripping experiments

Single dripping experiments were performed by pumping an oil fluid through the cylindrical inlet capillary and an aqueous solution through the outer square capillary, as indicated in Fig 1 (main manuscript). The inner and outer flow rates used for droplet formation were adjusted in the ranges of 50 and 40,000 μL/hr, respectively, using syringe pumps (Harvard apparatus, PHD 2000 Programmable, Holliston, MA, USA). In the case of experiments with a fluid

viscosity ratio $\tilde{\mu}$ of 4.6, the inner oil fluid was 1,6-hexanediol diacrylate (HDDA) (Sigma-Aldrich) and the outer fluid was an aqueous solution of 1% w/v poly(vinyl alcohol) (PVA) (M_W = 13000-23000 g/mol, 87% hydrolyzed, Sigma-Aldrich). For experiments with $\tilde{\mu}$ = 0.0005, the inner fluid was an oil mixture consisting of 3% w/v glycidyl methacrylate (97%, Sigma-Aldrich), 5% w/v dimethacrylate ethylene glycol (98%, Sigma Aldrich), 5% w/v Irgacure 907 (Photoinitiator, BASF) and 87% w/v methyl methacrylate (99%, Sigma-Aldrich); and the outer aqueous fluid was an aqueous solution of 2% w/v methyl cellulose (Sigma-Aldrich) in deionized water.

Multiple dripping was possible by pumping a third fluid from the other end of the square capillary, as illustrated in Fig. 3 (main manuscript). In this case, an aqueous solution of 2% w/v poly(vinyl alcohol) (PVA) (M_W = 13000-23000 g/mol, 87% hydrolyzed, Sigma-Aldrich) was pumped through the inlet capillary (phase 1), an oil solution of isobornyl acrylate (Sigma-Aldrich) with 3% w/v Span 85 (Sigma-Aldrich) was added through the square capillary so as to engulf the co-flowing inner aqueous solution (phase 2) and another aqueous solution of 2% w/v poly(vinyl alcohol) (PVA) was pumped through the square capillary in the opposite direction (phase 3, see Fig. 3 in the main manuscript).

In single and multiple dripping experiments, droplets are collected in the collector capillary. In our dripping experiments, droplet break-off occurs before the size of the droplet reaches the diameter of the collector capillary. In the limit of droplet sizes approaching the diameter of the collector capillary, the outer fluid velocity becomes increasingly large until the applied shear is sufficient to break off the droplet. We observe that break-off generally occurs at the collecting capillary orifice. This is not the case for the multiple dripping experiments, where droplet rupture occurs well into the collector capillary. This was taken into account by increasing the D_c term by 10% consistent with experimental video results.

Note that the dripping mode investigated here differs significantly from that where the droplet diameter is larger than the diameter of the collecting channel. In this regime, known as "mode 1" [2] or geometry-defined dripping, [3] the droplet size is somewhat independent of flow rates, viscosities, or interfacial tensions.

III. Measurement of Fluid Viscosities and Surface Tensions

The viscosities were measured using both an Ubbelohde viscometer and a double-gap Couette tool in a stress-controlled rheometer (Gemini Advanced Rheometer, Bohlin Instruments) at shear rates between 400-7500 s^{-1}. The interfacial tension between the different investigated fluids for the case of $\tilde{\mu}$ = 0.0005 was measured using the pendant drop technique (Profile Analysis Tensiometer, Sinterface). The surface tension was measured using pure water and using the methyl cellulose aqueous solution. In both cases, the surface tension was found to be 8.5 mN/m, indicating that this polymer is not surface active.

IV. Comparison of Shear Stress at the Droplet Surface with and without boundary conditions

To obtain an analytic expression for the size of droplets made by dripping in our microfluidic devices, we made certain simplifications to the complex flow patterns around the droplet protruding from the inlet capillary tip. Specifically, we assumed that the droplet experiences a Stokes drag-type shear force according to the average velocity of the encompassing fluid, $\overline{v}_2$. Using the Stokes drag equation for a rigid sphere in an infinite moving fluid to describe the flow pattern around the droplet enables size prediction using a simple analytic expression, but neglects two important boundary conditions of the system. The first boundary condition requires that there is no slip at the collector capillary wall and this should increase the shear stress on the droplet surface. The second boundary condition requires that the shear stress applied on the droplet surface is partially attenuated due to internal flow of the droplet fluid, decreasing the shear stress on the droplet. Here, we show that the stress enhancement caused by the non-slip condition at the capillary wall is roughly compensated by the stress attenuation resulting from internal flow of the droplet fluid. To evaluate if these two phenomena approximately offset each other such that the simplified drag force used in our model yields the correct scaling law for the droplet sizes within the studied parameter range, we estimate the shear stresses at the center circumference of the droplet for two different scenarios as depicted in Supplementary Figure 1.

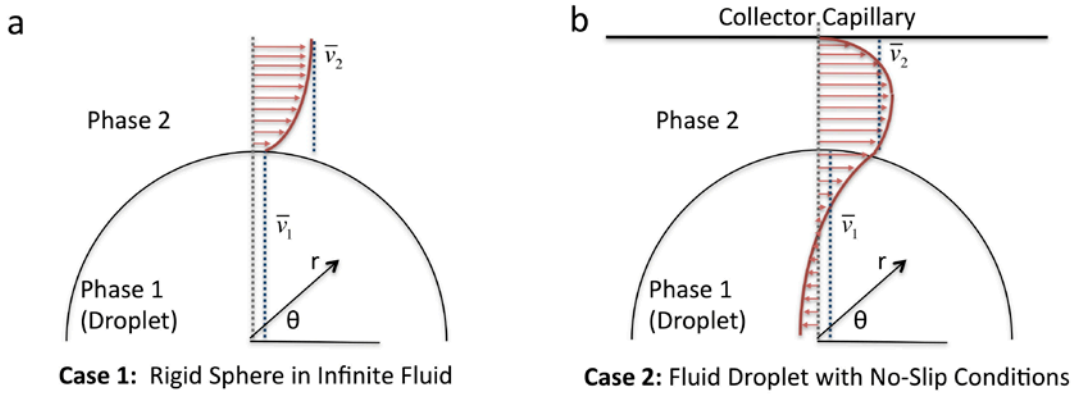

Supplementary Figure 1 – Approximate flow velocity profiles for the cases of a) a rigid sphere in an infinite fluid, and b) a fluid droplet taking into account no-slip conditions at the interfaces.

Case 1: Shear Stress on a rigid sphere in an infinite flowing fluid of velocity v_2

The well-known analytic expression for the velocity flow field around a rigid sphere in an infinite flowing fluid is given as: [4]

(S1)

$$v_r(r,\theta) = v_\infty\left(1 - \frac{3d}{4r} + \frac{d^3}{16r^3}\right)\cos\theta$$

$$v_\theta(r,\theta) = -v_\infty\left(1 - \frac{3d}{8r} - \frac{d^3}{32r^3}\right)\sin\theta.$$

where $v_\infty = \bar{v}_2 - \bar{v}_1$, the difference between the average flow velocities of phase 2 and 1. Here r represents the distance away from the center of the droplet and θ represents the angle away from the centerline of the capillary as shown in Supplementary Figure 1. The velocity profile at the center circumference of the droplet can be solved for by taking θ=90° and arriving at the expression:

$$v_2(r) = (\bar{v}_2 - \bar{v}_1)\left(1 - \frac{3d}{8r} - \frac{d^3}{32r^3}\right) \quad \text{(S2)}$$

This velocity profile is shown in Supplementary Figure 2a. The profile matches the trend expected in Supplementary Figure 1 and can be used to approximate the shear stress at the center circumference of the particle according to:

$$\tau = \mu_2\left(\partial v_2 / \partial r\right)\Big|_{r=d/2} = 3\mu_2(\bar{v}_2 - \bar{v}_1)d^{-1} \quad \text{(S3)}$$

This shear stress is plotted against an increasing droplet diameter for two different flow rates in Supplementary Figure 3.

Case 2: Shear Stress on a fluid droplet in a capillary assuming pipe flow of outer fluid

In case 2, we describe the velocity flow profile along the center of the droplet by taking into account a droplet-fluid interface and a no-slip condition at the wall of the collector capillary. To solve for the velocity profiles in the encompassing fluid, we make an *ansatz* that is motivated by the general solution for a flow in a circular pipe with three unknown coefficients as:

$$v_2(r) = A_2 r^2 + B_2 \log r + C_2. \quad \text{(S4)}$$

For the velocity profile within the droplet, we use a quadratic *ansatz* that approximates the expected flow profile shown in supplementary figure 1

$$v_1(r) = A_1 r^2 + C_1 \quad \text{(S5)}$$

The unknown coefficients can be derived from the no-slip boundary condition at the collector wall, the no-slip and continuous shear stress conditions across the fluid interface and two mass balance equations as:

$$v_2(r = D_c/2) = 0 \qquad \text{(S6)}$$
$$v_2(r = d/2) = v_1(r = d/2)$$
$$\mu_2(\partial v_2/\partial r)\big|_{r=d/2} = \mu_1(\partial v_1/\partial r)\big|_{r=d/2}$$
$$\int_{d/2}^{D_c/2} v_2(r)2\pi r\,dr = Q_2$$
$$\int_{0}^{d/2} v_1(r)2\pi r\,dr = Q_1$$

To satisfy these five equations, the coefficients must equal the following values:

$$B_2 = \frac{4}{\pi}\frac{Q_2\left(d^2 - D_c^2 - \frac{1}{2}d^2\,\mu_2/\mu_1\right) - Q_1\left(D_c^2 - \frac{1}{2}D_c^4/d^2 - \frac{1}{2}d^2\right)}{\left(\log\frac{1}{2}D_c - \log\frac{1}{2}d + \frac{1}{4}\mu_2/\mu_1\right)\left(d^2D_c^2 - \frac{1}{2}D_c^4 - \frac{1}{2}d^4\right) + \left(d^2 - D_c^2 - \frac{1}{2}d^2\,\mu_2/\mu_1\right)\left(d^2\left(\log\frac{1}{2}D_c - \log\frac{1}{2}d\right) - \frac{1}{2}D_c^2 + \frac{1}{2}d^2\right)} \qquad \text{(S7)}$$

$$A_2 = 4\frac{B_2\left(-\log\frac{1}{2}d + \log\frac{1}{2}D_c + \frac{1}{4}\mu_2/\mu_1\right) + 4Q_1/\pi d^2}{d^2 - D_c^2 - \frac{1}{2}d^2\,\mu_2/\mu_1}$$

$$C_2 = -\frac{1}{4}A_2D_c^2 - B_2\log\frac{1}{2}D_c$$

$$A_1 = (\mu_2/\mu_1)\left(A_2 + 2B_2/d^2\right)$$

$$C_1 = \frac{4Q_1}{\pi d^2} - \frac{1}{8}A_1d^2$$

The velocity profiles in the encompassing fluid and droplet are plotted for an example flow rate and droplet size in Supplementary Figure 2b and correlate well with the expected trends of Supplementary Figure 1b. With the velocity profiles known, the shear stress can be calculated according to:

$$\tau = \mu_1\left(\partial v_1/\partial r\right)\big|_{r=d/2} = \mu_1A_1d \qquad \text{(S8)}$$

This shear stress is plotted against an increasing droplet diameter for the same two flow rates as Case 1 in Supplementary Figure 3. Comparing the curves for cases 1 and 2 shows (a) that the shear stress at the droplet surface is under-predicted by our simplified model by about a factor of 10 and (b) that for both models the shear stress depends in nearly the same way on the droplet diameter (at least within the studied parameter ranges). This correspondence suggests that assuming much simpler flow conditions can be justified to be able to arrive at a scaling law to

predict droplet sizes made by dripping in our microfluidic devices. The apparent underestimation of the drag force is compensated in our scaling law by an appropriate choice of Ca_{crit}.

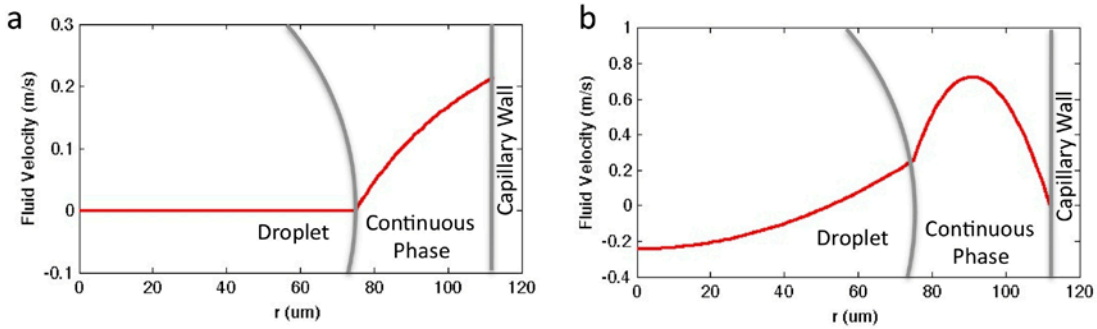

Supplementary Figure 2 – Derived velocity profiles for the center plane of the droplet for a) case 1 and b) case 2.

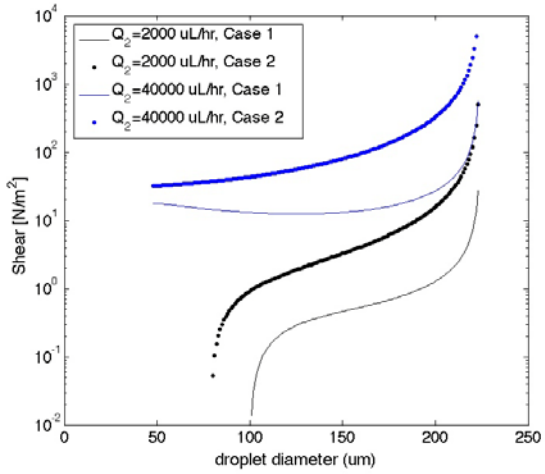

Supplementary Figure 3 – Comparison of shear stresses calculated for cases 1 and 2 across different droplet sizes for two diverse flow rates. The trends in the more accurate case 2 are captured with the simple expressions in case 1, enabling the derivation of an analytic expression based on the simpler flow pattern of case 1.

V. Critical Capillary Number for Isolated Droplets

In contrast to the rough approximation of Ca_{crit}=1 currently used in co-flowing geometries, [5] experimental and theoretical work on isolated spherical droplets offers more precise estimates. In this case, isolated droplets dispersed in a continuous fluid and subjected to various types of flow become unstable and rupture at critical Capillary numbers, Ca_{crit}, different from 1, as shown in Supplementary Figure 4 [6,7].

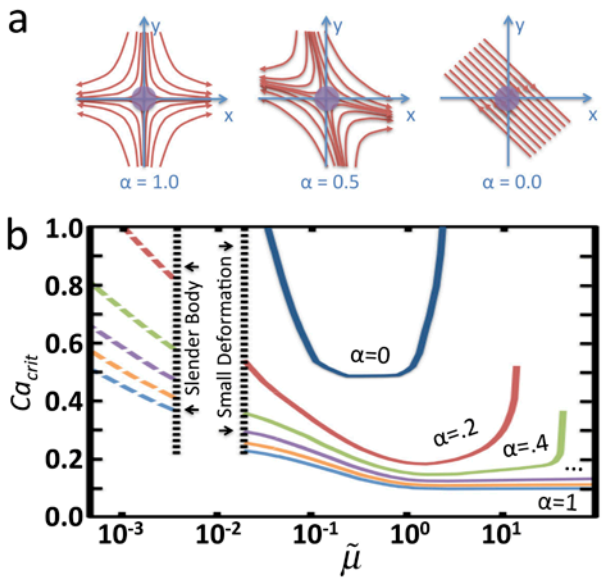

Supplementary Figure 4 – a) Stream lines (red) in flow systems ranging from simple shear (α=0) to purely extensional flow (α=1). b) The Ca_{crit} required in different α for the breakup of isolated droplets as a function of the ratio of fluid viscosities, $\tilde{\mu} = \mu_1/\mu_2$. μ_1 and μ_2 are the viscosities of the dispersed and continuous phases, respectively. Solid and dashed lines are obtained using small and large deformation theory, respectively. Adapted from [6] and [7].

Under low shear stresses ($Ca < Ca_{crit}$), an isolated droplet deforms until the interfacial tension associated with its surface balances the shear stress exerted by the continuous fluid, reaching a steady-state condition. For higher shear stresses ($Ca \geq Ca_{crit}$), the droplet exhibits a non-spherical unstable geometry that ultimately leads to rupture into smaller droplets. The Ca_{crit} for isolated droplets depends on the ratio of fluid viscosities, $\tilde{\mu} = \mu_1/\mu_2$, and on the flow conditions, as shown in the Supplementary Figure 4. The flow condition is expressed by α, (in accordance with [7]), so that $\alpha = 0$ for simple shear and $\alpha = 1$ for purely extensional flow. Two different regimes are observed in this figure. For $\tilde{\mu} >> 10^{-2}$, droplet rupture is described by small deformation theory [8]. For $\tilde{\mu} << 10^{-2}$, Taylor [9] and Buckmaster [10] pioneered slender body theory to explain the increased resistance to rupture for droplets made out of low-viscosity fluids dispersed in a highly viscous continuous phase [11]. Both small deformation and slender body theory have been validated in their current state through careful experimentation [7].

Remarkably, we find that experimental Ca_{crit} values based on Eq. 4 and determined experimentally in microcapillaries correspond extraordinarily well to the Ca_{crit} values predicted for isolated droplets under purely extensional flow. These results suggest that the flow around the capillary tip in flow-induced dripping has a predominantly extensional character, which is in agreement with previous numerical simulations. [12]

VI. Calculation of refraction correction in measuring inner droplet diameters (d_1) for multiple drippings

Observation of fluid droplets encapsulated in other fluid droplets, such as in multiple dripping systems, leads to refractive effects derived from the refractive index and density mismatches between the inner and outer phases. In the system studied here, sedimentation of the phase 1 droplet was observed in the phase 2 droplet due to a density mismatch. By taking this into account, as shown in Supplementary Figure 5, the actual diameter of the phase 1 dripping can be more accurately determined. The refractive correction for the diameter of the inner droplet was ~15%.

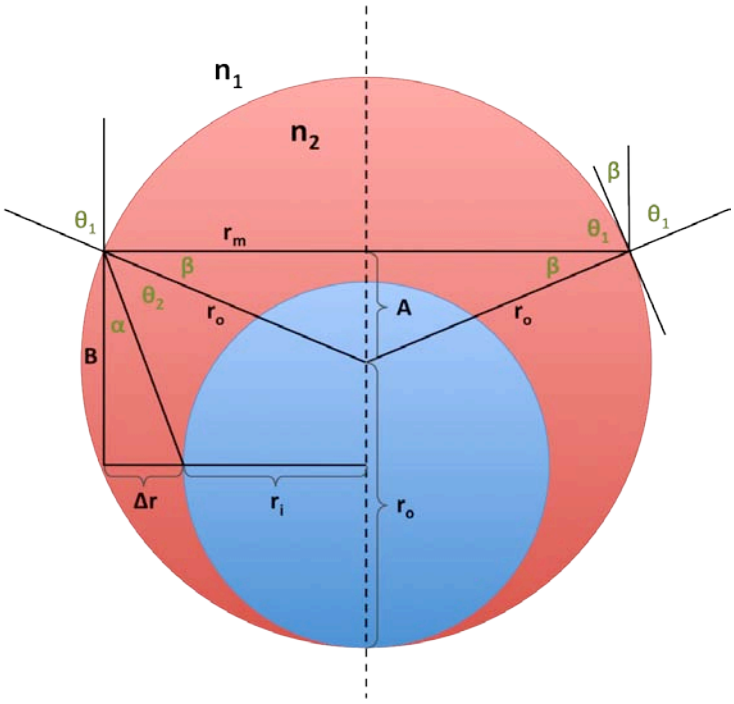

Supplementary Figure 5 - Schematic of a multiple dripping assembly. The observed diameter of the inner droplet ($d_1=2r_1$) is larger than the true diameter due to refractive effects.

In this calculation, all droplets are considered spherical and the inner droplet sits centered at the bottom of the outer droplet. Table I lists the additional parameters used in the calculation.

Table I: Parameters used to calculate the actual diameter of inner droplets in multiple dripping assemblies

parameter	**description**	**value**
n_1	refractive index of outer and inner phases (water)	1.33
n_2	refractive index of middle phase	1.476
r_o	measured outer radius	
r_m	measured inner radius	
r_i	actual inner radius	
Δr	difference between r_m and r_i	
θ_1	angle of incidence	
θ_2	angle of refraction	
α_o	auxiliary angle	
β_o	auxiliary angle	
A	auxiliary distance	
B	auxiliary distance	

Calculation of the actual inner radius is possible by considering the following geometric equations:

$$\beta_o = \cos^{-1}\left(\frac{r_m}{r_o}\right) \qquad (S9)$$

$$\theta_1 = 90° - \beta_o \qquad (S10)$$

$$\theta_2 = \sin^{-1}\left(\frac{n_1}{n_2}\cdot\sin\theta_1\right) \qquad (S11)$$

$$\alpha_o = 90° - \beta_o - \theta_2 \qquad (S12)$$

$$A = r_o \cdot \sin\beta_o \qquad (S13)$$

$$B = A + r_o - r_i \qquad (S14)$$

$$\Delta r = B \cdot \tan\alpha_o \qquad (S15)$$

$$r_i = r_m - \Delta r \qquad (S16)$$

Here, equation (S11) represents Snell's law. Combining these equations, we obtain the following relation between the actual inner radius and the observed radius:

$$r_i = \frac{r_m - r_0\left(1+\sqrt{1-\left(\frac{r_m}{r_o}\right)^2}\right)\tan\left[\frac{\pi}{2}-\cos^{-1}\left(\frac{r_m}{r_o}\right)-\sin^{-1}\left(\frac{r_m n_1}{r_o n_2}\right)\right]}{1-\tan\left[\frac{\pi}{2}-\cos^{-1}\left(\frac{r_m}{r_o}\right)-\sin^{-1}\left(\frac{r_m n_1}{r_o n_2}\right)\right]} \quad \text{(S16)}$$

References

1. A. S. Utada, E. Lorenceau, D. R. Link, P. D. Kaplan, H. A. Stone and D. A. Weitz, *Science*, 2005, **308**, 537-541.
2. Z. Nie, M. Seo, S. Xu, P. C. Lewis, M. Mok, E. Kumacheva, G. M. Whitesides, P. Garstecki and H. A. Stone, *Microfluid Nanofluid*, 2008, **5**, 585-594.
3. G. F. Cristopher and S. L. Anna, *Journal of Physics D*, 2007, **40**, R319-R336.
4. F. Durst, *Fluid mechanics: an introduction to the theory of fluid flows*, Springer-Verlag, Heidelberg, 2008.
5. P. B. Umbanhowar, V. Prasad and D. A. Weitz, *Langmuir*, 2000, **16**, 347-351.
6. H. A. Stone, *Annual Review of Fluid Mechanics*, 1994, **26**, 65-102.
7. B. J. Bentley and L. G. Leal, *Journal of Fluid Mechanics*, 1986, **167**, 241-283.
8. J. M. Rallison, *Journal of Fluid Mechanics*, 1980, **98**, 625-633.
9. G. I. Taylor, *Proc. Int. Congr. Appl. Mech.*, 1964, **11th**, 790-796.
10. J. D. Buckmaster, *Journal of Fluid Mechanics*, 1972, **55**, 385-400.
11. E. J. Hinch and A. Acrivos, *Journal of Fluid Mechanics*, 1978, **91**, 401-414.
12. R. Suryo and O. A. Basaran, *Physics of Fluids*, 2006, **18**.